

Article

Deep Learning for the Classification of Small-Cell and Non-Small-Cell Lung Cancer

Mark Kriegsmann ^{1,2,*}, Christian Haag ^{1,3}, Cleo-Aron Weis ⁴, Georg Steinbuss ^{1,3}, Arne Warth ⁵, Christiane Zgorzelski ¹, Thomas Muley ^{2,6}, Hauke Winter ^{2,6}, Martin E. Eichhorn ^{2,6}, Florian Eichhorn ^{2,6}, Joerg Kriegsmann ^{7,8}, Petros Christopolous ^{2,9}, Michael Thomas ^{2,9}, Mathias Witzens-Harig ¹⁰, Peter Sinn ¹, Moritz von Winterfeld ¹, Claus Peter Heussel ^{2,11,12}, Felix J. F. Herth ^{2,13}, Frederick Klauschen ¹⁴, Albrecht Stenzinger ^{1,2} and Katharina Kriegsmann ^{3,*}

¹ Institute of Pathology, Heidelberg University, 69120 Heidelberg, Germany; christian.haag@klinikum-bayreuth.de (C.H.); georg.steinbuss@med.uni-heidelberg.de (G.S.); christiane.zgorzelski@med.uni-heidelberg.de (C.Z.); peter.sinn@med.uni-heidelberg.de (P.S.); moritz.vonwinterfeld@med.uni-heidelberg.de (M.v.W.); albrecht.stenzinger@med.uni-heidelberg.de (A.S.)

² Translational Lung Research Centre Heidelberg, Member of the German Centre for Lung Research (DZL), 69120 Heidelberg, Germany; thomas.muley@med.uni-heidelberg.de (T.M.); hauke.winter@med.uni-heidelberg.de (H.W.); martin.eichhorn@med.uni-heidelberg.de (M.E.E.); florian.eichhorn@med.uni-heidelberg.de (F.E.); Petros.Christopolous@med.uni-heidelberg.de (P.C.); michael.thomas@med.uni-heidelberg.de (M.T.); felix.herth@med.uni-heidelberg.de (F.J.F.H.)

³ Department Hematology, Oncology and Rheumatology, Heidelberg University, 69120 Heidelberg, Germany; katharina.kriegsmann@med.uni-heidelberg.de

⁴ Institute of Pathology, University Medical Centre Mannheim, Heidelberg University, 68782 Mannheim, Germany; Cleo-Aron.Weis@medma.uni-heidelberg.de

⁵ Institute of Pathology, Cytopathology, and Molecular Pathology, UEGP MVZ Gießen/Wetzlar/Limburg; 65549 Limburg, Germany Warth@patho-uegp.de

⁶ Department of Thoracic Surgery, Thoraxklinik, Heidelberg University, 69126 Heidelberg, Germany

⁷ Molecular Pathology Trier, 54296 Trier, Germany; kriegsmann@patho-trier.de

⁸ Danube Private University Krems, 3500 Krems, Austria

⁹ Department of Thoracic Oncology, Thoraxklinik, Heidelberg University, 69126 Heidelberg, Germany

¹⁰ Medical Faculty Heidelberg University, 69120 Heidelberg, Germany; witzens.harig@yahoo.de

¹¹ Department of Diagnostic and Interventional Radiology with Nuclear Medicine, Thoraxklinik, Heidelberg University, 69120 Heidelberg, Germany

¹² Department of Diagnostic and Interventional Radiology, Thoraxklinik, Heidelberg University, 69120 Heidelberg, Germany

¹³ Department of Pneumology and Critical Care Medicine, Thoraxklinik, Heidelberg University, 69126 Heidelberg, Germany

¹⁴ Institute of Pathology, University Hospital Charité, 10117 Berlin, Germany; frederick.klauschen@charite.de

* Correspondence: mark.kriegsmann@med.uni-heidelberg.de (M.K.); katharina.kriegsmann@med.uni-heidelberg.de (K.K.); Tel.: +49 6221 56 36930 (M.K.); +49 6221 56 37238 (K.K.)

Received: 7 June 2020; Accepted: 15 June 2020; Published: 17 June 2020

Abstract: Reliable entity subtyping is paramount for therapy stratification in lung cancer. Morphological evaluation remains the basis for entity subtyping and directs the application of additional methods such as immunohistochemistry (IHC). The decision of whether to perform IHC for subtyping is subjective, and access to IHC is not available worldwide. Thus, the application of additional methods to support morphological entity subtyping is desirable. Therefore, the ability of convolutional neuronal networks (CNNs) to classify the most common lung cancer subtypes, pulmonary adenocarcinoma (ADC), pulmonary squamous cell carcinoma (SqCC), and small-cell lung cancer (SCLC), was evaluated. A cohort of 80 ADC, 80 SqCC, 80 SCLC, and 30 skeletal muscle specimens was assembled; slides were scanned; tumor areas were annotated; image patches were extracted; and cases were randomly assigned to a training, validation or test set. Multiple CNN architectures (VGG16, InceptionV3, and InceptionResNetV2) were trained and optimized to classify the four entities. A quality control (QC) metric was established. An optimized InceptionV3 CNN

architecture yielded the highest classification accuracy and was used for the classification of the test set. Image patch and patient-based CNN classification results were 95% and 100% in the test set after the application of strict QC. Misclassified cases mainly included ADC and SqCC. The QC metric identified cases that needed further IHC for definite entity subtyping. The study highlights the potential and limitations of CNN image classification models for tumor differentiation.

Keywords: Artificial intelligence; deep learning; lung cancer; histology; non-small cell lung cancer; small cell lung cancer

1. Introduction

Based on the GLOBOCAN 2018 produced by the International Agency for Research on Cancer, a database that estimates the incidence and mortality of cancer (including 185 countries and 36 cancers), lung cancer incidence is high and was estimated to be 2.1 million new cases and 1.8 million deaths worldwide, representing 18.4% of all cancer cases [1]. Thus, lung cancer is the most common cancer type among men and the third most common in women worldwide [2]. Smoking is the major risk factor for lung cancer. The 20-fold variation in lung cancer rates in different regions/countries reflects the differences in smoking habits as well as the intensity and type of cigarettes [2,3]. Despite major advances in diagnostics and therapy, mortality remains high, with a five-year tumor-associated mortality of 19%.

Clinical management highly depends on the histological subtype, as well as immunohistological (IHC) and genetic tumor characteristics [4]. Two major categories are discerned—small-cell lung cancer (SCLC) and non-small-cell lung cancer (NSCLC). The first category constitutes approximately 15%, and the second is responsible for approximately 85% of tumors. The two most common entities in the NSCLC category are pulmonary adenocarcinoma (ADC) and pulmonary squamous cell carcinoma (SqCC), which make up approximately 90% of all NSCLC [5]. Lung cancer is highly heterogeneous, which is reflected by the underlying genetic aberrations that have been detected in the past decades [4,6]. At an advanced clinical stage, individualized therapy highly depends on genetic aberrations involving EGFR, BRAF, ALK, ROS1, RET, etc. [7]. Moreover, the introduction of immune checkpoint and kinase inhibitors has improved prognosis for patients without genetic alterations in these target genes [8,9].

Morphological evaluation of tissue sections remains the basis of histopathological diagnostics and directs the application of additional analyses [10]. In some tumors, the diagnosis can be established on morphology alone, but in a subset of cases, IHC stains are required for definitive diagnosis [11,12]. Currently, the decision of whether to perform IHC is subjective. Moreover, some pathologists can rely on expensive and methodological equipment that allows for liberal use of IHC, while others cannot [13]. Thus, additional methods that support morphological entity subtyping are desirable.

Digital pathology has emerged as an important tool, not only to review histopathological slides on a computer but also to use additional computer-assisted software to support routine diagnostics and research [14–17]. A prominent example is the evaluation of the intensity and extent of IHC staining that can be assessed by various software applications. It has been shown that proliferative activity can reliably be assessed by computer-assisted evaluation, which in turn supports routine diagnostics in tumors where the proliferation rate plays a major role, such as in neuroendocrine neoplasms [18–20]. With these tools, one can extract detailed morphometric information from cells that, after training, allows for automatic detection of tumor and stromal cells [21]. However, as the architectural arrangement of cells is commonly neglected using this approach, different tumor types cannot reliably be differentiated. An alternative approach that allows one to take the architectural pattern into account is the application of convolutional neuronal networks (CNNs) [22,23].

In this study, we applied CNNs and evaluated their capability to classify the most common lung cancer subtypes—namely, SCLC, ADC, and SqCC. Moreover, we developed quality control (QC) measures to objectively detect cases that should be submitted for further evaluation.

2. Methods

2.1. Patient Cohort, Tissue Microarray Construction, and Scanning of Tissue Slides

A cohort of the three most frequent lung cancer subtypes—SCLC ($n = 80$), ADC ($n = 80$) and SqCC ($n = 80$)—and skeletal muscle ($n = 30$) as a control was assembled from the archive from the Institute of Pathology, University Clinic Heidelberg with the support of the Tissue Biobank of the National Center for Tumor Diseases (NCT). Diagnoses were made according to the 2015 World Health Organization Classification of Tumors of the Lung, Pleura, Thymus, and Heart [12]. In brief, conventional Hematoxylin and Eosin staining as well as immunohistochemistry according to current best practice recommendations were performed [24]. Diagnosis of SCLC was established by morphology as well as through expression of neuroendocrine markers such as synaptophysin, chromogranin and CD56 [25]. Diagnosis of ADC was made if the tumor exhibited growth patterns typical for ADC such as lepidic, acinar, papillary or micropapillary; showed intracytoplasmic reactivity in the Periodic acid–Schiff stain and/or showed immunoreactivity of thyroid transcription factor 1 (TTF-1). Diagnosis of SqCC was rendered if the tumor exhibited intercellular bridges and/or keratinization on morphology, as well as absence of TTF-1 staining and positivity of p40 in more than 50% of tumor cell nuclei using IHC [26]. The study was approved by the local ethics committee (#S-207/2005 and #S315/2020). Formalin-fixed, paraffin-embedded tissue blocks were extracted, and a tissue microarray (TMA) was built as previously described [18,26–28]. TMAs were scanned at 400x magnification using a slide scanner (Aperio SC2, Leica Biosystems, Nussloch, Germany).

2.2. Tumor Annotation and Image Patch Extraction

Scanned slides were imported into QuPath (v.0.1.2, University of Edinburgh, Edinburgh, UK). Tumor areas of SCLC, ADC, and SqCC as well as from skeletal muscle were annotated by a pathologist (M.K.). Patches $100 \times 100 \mu\text{m}$ ($395 \times 395 \text{ px}$) in size were generated within QuPath, and the tumor-associated image patches were exported to the local hard drive [21]. To ensure adequate representation of each tumor, the goal of exporting a minimum of 10 patches per patient was set. Representative tumor areas, tumor annotations, generated patches, and extracted patches are displayed (Figures 1 and 2).

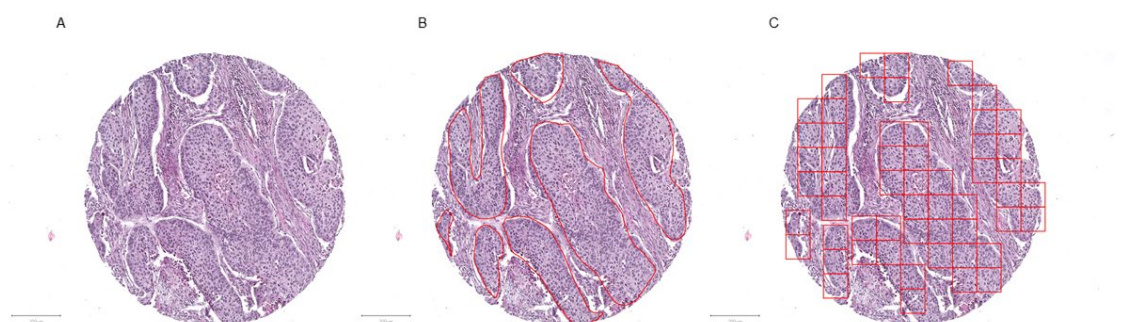


Figure 1. Tumor annotation and generation of image patches. Representative tissue microarray core of a squamous cell carcinoma without (A) and with annotation (B, red outline), as well as after image patches creation (C). The image patches were subsequently saved as .png files. Magnification or scale bars: $200 \mu\text{m}$

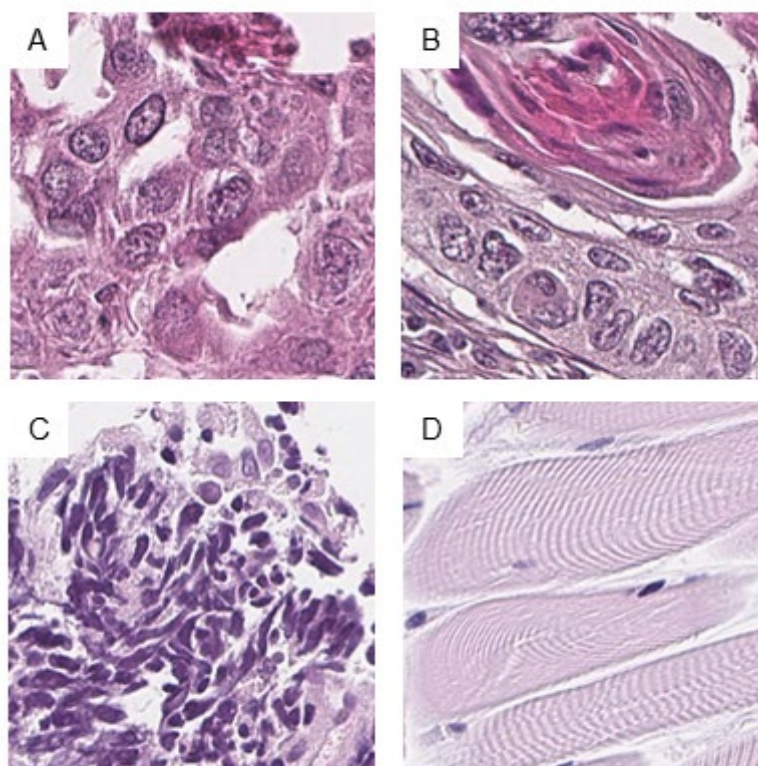


Figure 2. Examples of image patches from annotated areas. One representative image patch from adenocarcinoma (ADC) (A), squamous cell carcinoma (SqCC) (B), small-cell lung cancer (SCLC) (C), and skeletal muscle (D) is shown. Magnification or scale bars: each image $100 \times 100 \mu\text{m}$ ($395 \times 395 \text{ px}$).

2.3. Hardware and Software

The following hardware were used for all calculations: Lenovo Workstation p72, CPU Intel(R) Xeon(R) E-2186 M, 2.90 GHz (Intel, Santa Clara, CA, USA), GPU 128 GB DDR4 RAM, GPU NVIDIA Quadro P5200 with Max-Q Design 16 GB RAM (Nvidia, Santa Clara, CA, USA). The following software were used: x64 Windows for Workstations (Microsoft, Redmond, WA, USA), R (v.3.6.2, GNU Affero General Public License v3) and RStudio (v.1.2.5033, GNU Affero General Public License v3) with the packages Keras (v.2.2.5.0), TensorFlow (v.2.0.0) and Tidyverse (v.1.3.0).

2.4. Analytical Subsets

To ensure reliable results, image patches were randomly separated into training (60% of patients), validation (20% of patients), and test sets (20% of patients). All image patches from a patient were in one of the sets only. These subsets were not changed during the analyses.

2.5. Convolutional Neuronal Network

Our setup using keras and tensorflow in R analytical software allowed us to choose a subset of different network architectures among the hundreds of network architectures available. After a literature review, three different commonly used and previously published CNN architectures were chosen and applied for the analysis. The results were subsequently compared. The CNNs were VGG16, InceptionV3 and InceptionResNetV2 [29–35]. The size, Top-1 accuracy, Top-5 accuracy on the ImageNet validation dataset, the number of parameters and the depth of VGG16, InceptionV3 and InceptionResNetV2 are as follows: 528 Megabyte (MB), 0.713, 0.901, 138,357,544, 23; 92 MB, 0.779, 0.937, 23,851,784, 159, and 215 MB, 0.803, 0.953, 55,873,736, 572, respectively [36]. The top layer was

removed, and an additional network including a flattened layer, a dense layer composed of 256 neurons (ReLU activation function), and an output layer with four classes (Softmax activation function) was put on top of the convolutional base. The optimizer applied was RMSProp with a learning rate of 0.00002. All three network architectures were trained with and without pretrained weights from ImageNet. Different iteration numbers, input image sizes, batch sizes, and dropout rates were evaluated to find a reliable classification model for the training and validation sets. The best model was used to classify the test set.

3. Results

3.1. Patient Cohort, Annotation, Image Patches Extraction, and Subset Analysis

Cases from SCLC ($n = 80$), ADC ($n = 80$), SqCC ($n = 80$), and skeletal muscle ($n = 30$) were successfully identified, retrieved, assembled in a TMA, stained, and scanned. Identification of the tumor-containing region resulted in a total of 12,472 extracted $100 \times 100 \mu\text{m}$ ($395 \times 395 \text{ px}$) image patches. The aim of extracting at least 10 image patches per patient was achieved in all but three SCLC cases, which were still included in the analysis. The number of extracted patches is displayed in Table 1 and Figure 3. Table 1 shows the number of image patches in the training, validation and test sets (60%, 20%, and 20% of patients, respectively) after random patient-based selection.

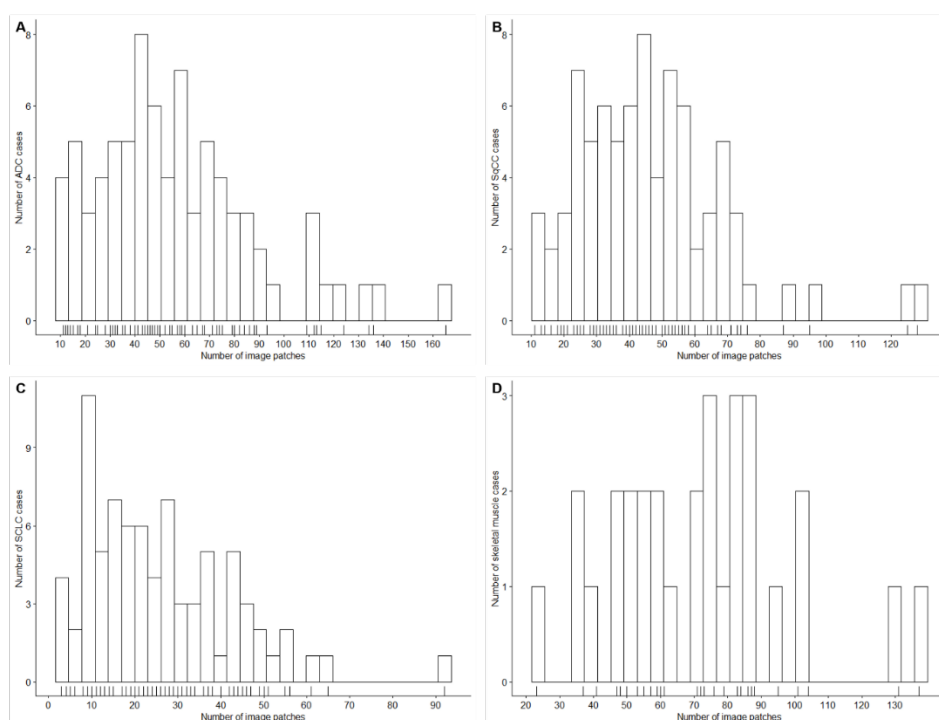


Figure 3. Number of patches according to the tissue type. The histograms show the number of annotated image patches for ADC (A), SqCC (B), SCLC (C), and skeletal muscle (D) cases.

Table 1. Descriptive statistics of annotated image patches and analysis subsets.

| Tissue Type | ADC | SqCC | SCLC | Skeletal Muscle | Overall Sum |
|--|------|------|------|-----------------|-------------|
| Overall Analysis set, 100% of Cases | | | | | |
| Cases, n | 80 | 80 | 80 | 30 | |
| Image patches, n | | | | | |
| Sum | 4505 | 3695 | 2075 | 2152 | 12,427 |
| Minimum | 11 | 11 | 3 | 23 | |
| Maximum | 165 | 128 | 92 | 137 | |
| Mean | 56 | 46 | 26 | 72 | |

| | | | | | |
|-------------------------------------|------|------|------|------|-------|
| Median | 51 | 43 | 23 | 73 | |
| Training Set, 60% of Cases | | | | | |
| Cases, <i>n</i> | 48 | 48 | 49 | 18 | |
| Image patches, <i>n</i> | | | | | |
| Sum | 2686 | 2108 | 1253 | 1298 | 7345 |
| Minimum | 11 | 13 | 3 | 37 | |
| Maximum | 165 | 95 | 92 | 131 | |
| Mean | 56 | 44 | 26 | 72 | |
| Median | 54 | 43 | 22 | 73 | |
| Validation Set, 20% of Cases | | | | | |
| Cases, <i>n</i> | 16 | 16 | 15 | 6 | |
| Image patches, <i>n</i> | | | | | |
| Sum | 871 | 845 | 437 | 479 | 2632 |
| Minimum | 15 | 11 | 4 | 37 | |
| Maximum | 136 | 128 | 65 | 137 | |
| Mean | 54 | 53 | 29 | 80 | |
| Median | 46 | 48 | 28 | 72 | |
| Test Set, 20% of Cases | | | | | |
| Cases, <i>n</i> | 16 | 16 | 16 | 6 | |
| Image patches, <i>n</i> | | | | | |
| Sum | 948 | 742 | 385 | 375 | 2450* |
| Minimum | 13 | 19 | 4 | 23 | |
| Maximum | 115 | 76 | 56 | 87 | |
| Mean | 59 | 46 | 24 | 63 | |
| Median | 55 | 41 | 23 | 70 | |

* Two image patches were removed at random to ensure divisibility by the batch size of 16 ($16 \times 153 = 2448$). ADC: adenocarcinoma; SqCC: squamous cell carcinoma; SCLC: small-cell lung cancer.

3.2. Convolutional Neuronal Network Selection and Hyperparameter Optimization

Comparison of CNN architectures trained with and without pretrained weights showed a distinct increase in classification accuracy in the former (Table 2A,B). Moreover, overfitting was apparent when more than 20 epochs were trained. Because the classification accuracies of InceptionV3 and InceptionResNetV2 were slightly better in the validation set and the training time was less with the InceptionV3 architecture compared to the InceptionResNetV2 architecture, all other optimization steps were done with the InceptionV3 architecture without pretrained weights and with 20 epochs.

Testing of different input image sizes of 128×128 px, 256×256 px, and 395×395 px revealed a classification accuracy of 83%, 95%, and 93% in the training set and 84%, 89%, and 84% in the validation set, respectively (Table 2C). An input size of 256×256 px showed the highest classification accuracy; therefore, this particular image size was chosen for further analysis.

Different batch sizes (8, 16, 32, and 64) were compared. A batch size of 16 had optimal classification accuracy metrics, i.e., 95% in the training set and 89% in the validation set (Table 2D).

As a slight overfitting was noted, different dropout rates (0, 0.1, 0.2, 0.3, 0.4, and 0.5) were evaluated. Compared with the other values, no overfitting was noted with a drop-out rate of 0.5 and a classification accuracy of 88% and 89% in the training and validation sets, respectively (Table 2E).

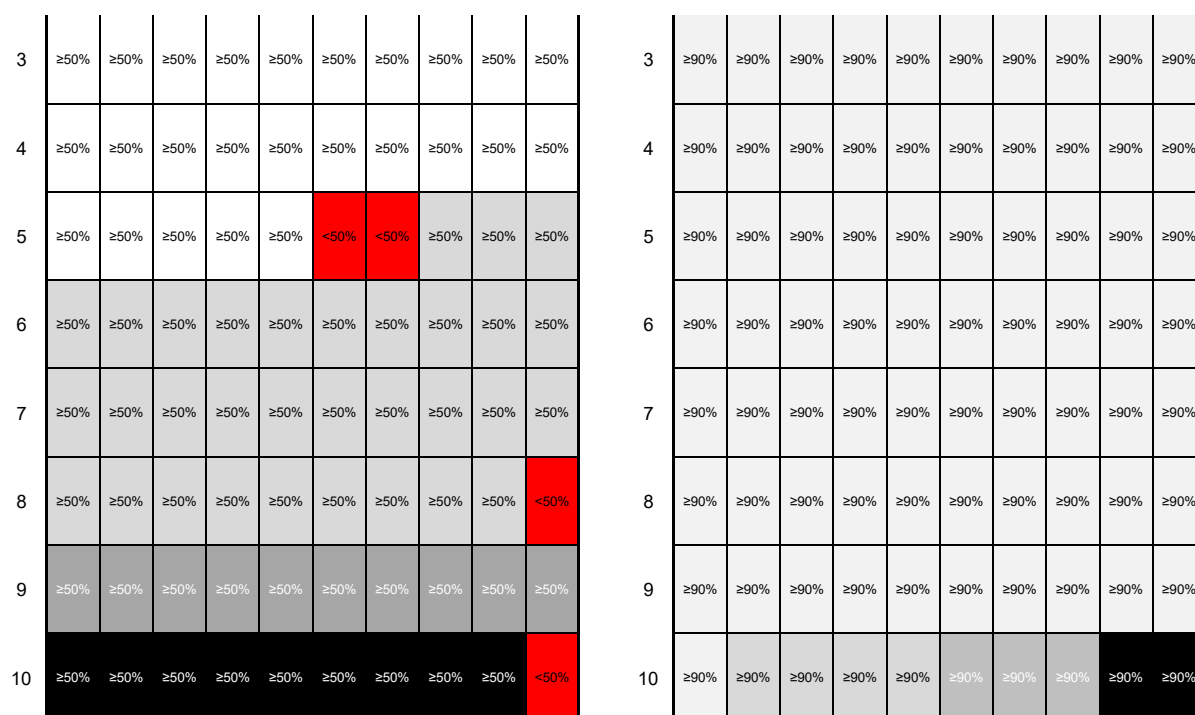


Figure 4. Principle of the introduced image patch and case quality control (QC). To demonstrate the general principle of the introduced QC, two examples—one for 50%/50% image patch/case QC (A) and one for 90%/90% image patch/case QC (B)—are shown. Given the rationale that a patient case would consist of 100 image patches, 50 and 90 image patches would need a probability of at least 50% (A) and 90% (B) to fall in a class. In the first example (A), 96 image patches have a $\geq 50\%$ probability to belong to one class (image QC passed in 96 image patches (different shades of grey correspond to the four classes) and failed in four image patches (red)). As $< 50\%$ of image patches belong to the class with the largest proportion (light grey), the case QC failed. In the second example (B) all image patches have a $\geq 90\%$ probability to belong to one class (image QC passed in all image patches). As $> 90\%$ of image patches belong to the class with the largest proportion (light grey), the case QC passed.

First, the image patch QC was increased from 50% to 90% in 10% increments. With increasing values for the image patch QC, the number of image patches that did not pass the QC increased from 1/2448 ($< 1\%$) at an image patch QC of 50% to 386/2448 (16%) at an image patch QC of 90%. Simultaneously, the classification accuracy increased from 89% to 95% in the whole cohort. Most misclassifications were found between ADC and SqCC (Table A1).

The classification results separated for the whole cohort, for the three lung cancer subtypes, and for the NSCLC subgroup are displayed in Table 3.

Table 3. Proportion of image patches with failed QC and classification accuracy according to image patch QC.

| Image Patch QC Value | Image Patches with Failed QC (n) | Proportion of Image Patches with Failed QC (%) | Classification Accuracy of ADC, SqCC, SCLC, Skeletal Muscle Image Patches (%) | Classification Accuracy of ADC, SqCC, SCLC Image Patches (%) | Classification Accuracy of ADC, SqCC Image Patches (%) |
|----------------------|----------------------------------|--|---|--|--|
| 50% | 1 | 0.04 | 89 | 87 | 85 |
| 60% | 79 | 3 | 91 | 89 | 87 |
| 70% | 150 | 6 | 92 | 90 | 89 |
| 80% | 255 | 10 | 93 | 92 | 90 |
| 90% | 389 | 16 | 95 | 94 | 92 |

The proportion of image patches with failed QC was calculated in all ADC, SqCC, SCLC, and skeletal muscle image patches of the test set ($n_{\text{overall}} = 2448$).

Second, case QC was evaluated in combination with image patch QC from 50% to 90% in 10% increments. The results for the whole cohort are displayed in Table 4A. Regardless of the combination of QC values, SCLC and skeletal muscle cases were always correctly classified. Thus, the classification accuracy for the whole cohort was better than that for the NSCLC subgroup. With increasing values for case QC, the number of patients who did not pass increased from 0% to 19% in the whole cohort. The classification results and the number/proportion of cases that did not pass the QC for the three lung cancer subtypes and for the NSCLC subgroup are displayed in Table 4B,C. In the NSCLC subgroup, a classification accuracy of 100% was achieved using image patch and case QCs of 90%. Using these parameters, 31% of cases did not pass QC.

Table 4. Classification accuracy and proportion of cases in which QC failed.

| Case QC Value | | 50% | | 60% | | 70% | | 80% | | 90% | |
|--|-----|--------|---------------|--------|---------------|--------|---------------|--------|---------------|--------|---------------|
| Parameter | | CA (%) | QC Failed (%) | CA (%) | QC Failed (%) | CA (%) | QC Failed (%) | CA (%) | QC Failed (%) | CA (%) | QC Failed (%) |
| A. ADC, SqCC, SCLC, and Skeletal Muscle Cases | | | | | | | | | | | |
| Image patch QC value | 50% | 94 | 0 | 96 | 6 | 98 | 11 | 100 | 19 | 100 | 24 |
| | 60% | 94 | 0 | 98 | 4 | 98 | 9 | 98 | 17 | 100 | 22 |
| | 70% | 94 | 0 | 98 | 6 | 98 | 9 | 98 | 15 | 100 | 20 |
| | 80% | 94 | 0 | 98 | 4 | 98 | 9 | 98 | 13 | 100 | 19 |
| | 90% | 96 | 0 | 98 | 4 | 98 | 7 | 98 | 9 | 100 | 19 |
| B. ADC, SqCC, and SCLC Cases | | | | | | | | | | | |
| Image patch QC value | 50% | 94 | 0 | 96 | 6 | 98 | 13 | 100 | 21 | 100 | 27 |
| | 60% | 94 | 0 | 98 | 4 | 98 | 10 | 97 | 19 | 100 | 25 |
| | 70% | 94 | 0 | 98 | 6 | 98 | 10 | 98 | 17 | 100 | 23 |
| | 80% | 94 | 0 | 98 | 4 | 98 | 10 | 98 | 15 | 100 | 21 |
| | 90% | 96 | 0 | 98 | 4 | 98 | 8 | 98 | 10 | 100 | 21 |
| C. ADC and SqCC Cases | | | | | | | | | | | |
| Image patch QC value | 50% | 91 | 0 | 93 | 9 | 96 | 19 | 100 | 31 | 100 | 41 |
| | 60% | 91 | 0 | 97 | 6 | 96 | 16 | 96 | 28 | 100 | 38 |
| | 70% | 91 | 0 | 97 | 9 | 96 | 16 | 96 | 25 | 100 | 34 |
| | 80% | 91 | 0 | 97 | 6 | 96 | 16 | 96 | 22 | 100 | 31 |
| | 90% | 94 | 0 | 97 | 6 | 96 | 13 | 96 | 16 | 100 | 31 |

The proportion of cases with failed QC was calculated in all ADC ($n = 16$), SqCC ($n = 16$), SCLC ($n = 16$) and skeletal muscle ($n = 6$) cases of the test set ($n = 54$).

4. Discussion

The morphological evaluation of tissue specimens in lung cancer diagnostics is the basis for further molecular testing and therapy stratification [12]. Criteria for additional IHC testing after morphological assessment are subjective. The combination of digital pathology and machine learning has the potential to support this decision process in an objective manner [37,38]. In a previous investigation, the application of deep learning to classify cytological preparations and histological specimens yielded promising results in various cancer types including lung cancer [39–41].

In this study, we analyzed whether a CNN-model (InceptionV3 CNN) could be used to differentiate the most common lung cancer subtypes—SCLC, ADC, and SqCC. To check the plausibility of the results, skeletal muscle was also included in the analysis. Histologically, the distinction of skeletal muscle and the three tumor entities is unambiguous. Furthermore, high classification accuracies were expected for the distinction between SCLC and NSCLC, as the cell size is commonly very different [12]. Only in unique cases can separation be difficult by morphology alone, e.g., when the tumor cell count is low, or in specimens with pronounced crush artifacts. The separation between ADC and SqCC is often possible by morphological evaluation alone, but in a subset of cases, only reliable if additional IHC stains are applied. Specifically, poorly differentiated

tumors require the use of IHC to identify metastases from extrapulmonary tumors [24,26,28,42,43]. Thus, it was expected that the classification accuracies would be high for skeletal muscle and SCLC but rather intermediate for ADC and SqCC.

In this study, we used a TMA to extract the image patches for several reasons. First, the tumor-containing area of each patient is comparable [18]. Second, the number of extracted image patches is limited, which saves computational resources. Third, the scan time and hard drive space is lower, and fourth, more tumors can be annotated at the same time by using whole slide annotations. Moreover, a TMA is suitable to mimic the biopsy situation [44]. Once the algorithm is trained, it can be applied to image patches extracted from TMAs, biopsies or resection specimens and therefore is in principle applicable in the routine setting.

The creation of image patches from a scanned image is necessary, as CNN can process only limited image sizes [45]. The separation of 60%, 20%, and 20% for the training, validation, and test sets was arbitrary, and there is currently no established gold standard [38,46–48]. A higher proportion of cases in the training set would result in a more robust model, but the data in the validation and test cohort would possibly not be representative. Nonetheless, separation into the three sets is mandatory, as during hyperparameter tuning, information from the training set migrates into the validation set. Thus, the capacity of the model must be tested on a separate test set.

In the past, various CNN architectures and modifications have been developed, and some show a high classification accuracy in the ImageNet dataset [49–51]. However, as the newer CNN architectures were not (yet) implemented in the software that was used here, we choose CNN architectures that were previously used to classify image data and were available in our software. Because it has been shown that the pretrained weights from the ImageNet dataset can also be used to efficiently classify new images, the CNN architectures were evaluated both with and without pretrained weights [38,46]. However, as the classification accuracy was distinctly lower with pretrained weights, we choose to use the CNN architectures without pretrained weights [38]. There is no established standard for the optimization process of a CNN model, but all parameters used in this study were within the range of reported variations [52–55].

The final model was robust and reached an image patch classification accuracy of 88% in the training as well as in the validation set which is comparable to previous studies using histological images [56,57]. Mainly ADC and SqCC were misclassified, as expected. For a routine application of a CNN for entity subtyping, a classification based on patients is much more meaningful. Therefore, the entity was defined by the proportion of image patches that were most common. As expected, a higher value for the QC resulted in a higher proportion of cases with a failed QC. Irrespective of the evaluated subset (whole cohort, three lung cancer subtypes or NSCLC cases), the classification accuracy increased to 100% using image patch and case QC cutoffs of 90%. For the ADC and SqCC subgroups, 31% of patients did not meet the QC criteria using image patch and case QC cutoffs of 90%. Thus, the CNN classification model and the subsequent application of QC measures allowed us to objectively identify cases that needed further IHC evaluation for definite entity subtyping.

The limitations of our study are the sample size, the number of extracted image patches in some cases, the number of included entities and the process for hyperparameter tuning. Herein, we examined 80 cases per lung cancer entity. Based on the random separation into training, validation and test sets, only 48 tumors were included in the training set. ADC and SqCC may be morphologically very different, and many variants are recognized in the current World Health Organization classification [12]. Furthermore, there may be mixed tumors such as SCLC combined with large cell neuroendocrine tumors or adenosquamous carcinomas [58,59]. Based on the broad biological variation, it becomes clear that the limited number of cases and extracted image patches per patient can only display a fraction of the possible morphological spectrum. Moreover, it is apparent that mixed tumors are a particular challenge for CNN-based classifications. Our model was trained to detect only the three most common lung cancer entities. Therefore, it cannot be expected that the CNN will reliably classify entities that were not trained, including other pulmonary or extrapulmonary tumors. Moreover, a small number of tumor cells per image patch may be a limiting factor and the minimal number of tumor cells needed for a reliable result is currently not clear. Thus,

additional QC measures merit further investigation. Based on the abovementioned statements, the application of CNN for tumor classification must always be conducted under the supervision of a pathologist to avoid misdiagnosis and potentially harmful consequences for patients. Finally, hyperparameter optimization was conducted sequentially. As not all possible hyperparameter combinations were tested, there is a possibility that there is an even better combination of hyperparameters. However, as hyperparameter tuning in our study resulted only in minor improvements, it was assumed that the influence of a better combination of hyperparameters would be minimal.

5. Conclusions

In summary, we trained and optimized a CNN model to reliably classify the three most common lung cancer subtypes. Moreover, we established QC measures to objectively identify cases that need further IHC validation for reliable entity subtyping. Our results highlight the potential and limitations of CNN image classification models for morphology-based tumor classification.

Author Contributions: M.K.: Conceptualization, Writing—original draft, Investigation, Supervision. C.H.: Formal analysis, Project administration, Writing—review and editing. C.A.W., G.S., A.W., C.Z.: Methodology, Writing—review and editing. T.M., H.W., M.E.E., F.E., J.K., P.C., M.T., M.W.H., P.S., M.v.W., C.P.H., F.J.F.H., F.K., A.S.: Resources, Writing—review and editing. K.K.: Formal analysis, Investigation, Visualization, Software, Writing—original draft. All authors have read and agreed to the published version of the manuscript.

Funding: This research received no external funding.

Acknowledgments: The Biobank of the National Centre for Tumor Diseases is kindly acknowledged.

Conflicts of Interest: The authors declare no conflict of interest.

Appendix A

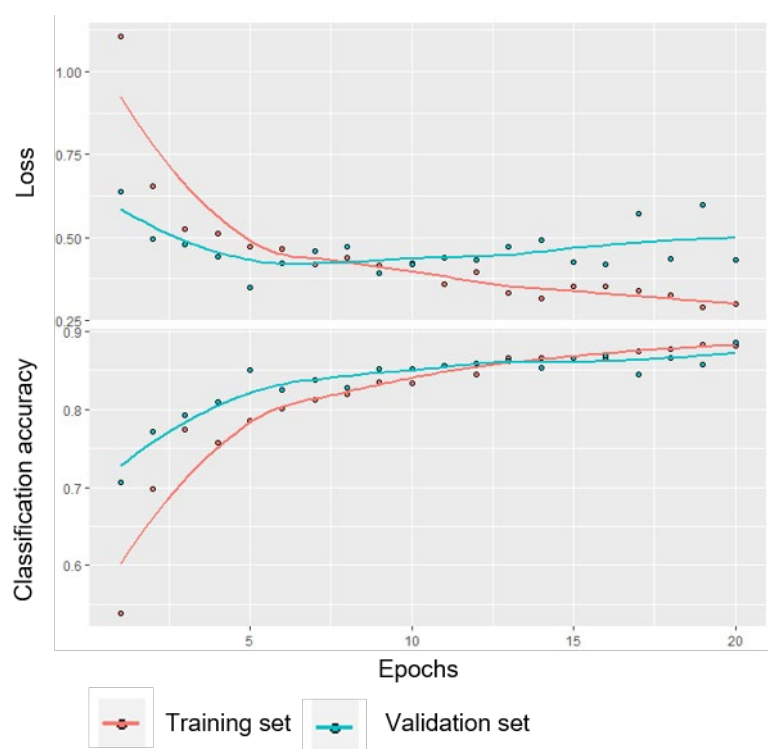


Figure A1. Loss and classification accuracy of the final CNN model.

Table A1. True and predicted diagnoses of test set image patches according to different image patch QC values.

| Image Patch QC Value | True Diagnosis | Predicted Diagnosis | | | | Image Patch QC Failed |
|----------------------|-----------------|---------------------|------|------|-----------------|-----------------------|
| | | ADC | SqCC | SCLC | Skeletal Muscle | |
| 50% | | | | | | |
| | ADC | 798 | 137 | 12 | 0 | 1 |
| | SqCC | 116 | 624 | 0 | 0 | 0 |
| | SCLC | 0 | 0 | 385 | 0 | 0 |
| | Skeletal muscle | 0 | 0 | 0 | 375 | 0 |
| 60% | | | | | | |
| | ADC | 776 | 109 | 12 | 0 | 51 |
| | SqCC | 101 | 611 | 0 | 0 | 28 |
| | SCLC | 0 | 0 | 385 | 0 | 0 |
| | Skeletal muscle | 0 | 0 | 0 | 375 | 0 |
| 70% | | | | | | |
| | ADC | 753 | 86 | 12 | 0 | 97 |
| | SqCC | 89 | 598 | 0 | 0 | 53 |
| | SCLC | 0 | 0 | 385 | 0 | 0 |
| | Skeletal muscle | 0 | 0 | 0 | 375 | 0 |
| 80% | | | | | | |
| | ADC | 721 | 66 | 11 | 0 | 150 |
| | SqCC | 71 | 564 | 0 | 0 | 105 |
| | SCLC | 0 | 0 | 385 | 0 | 0 |
| | Skeletal muscle | 0 | 0 | 0 | 375 | 0 |
| 90% | | | | | | |
| | ADC | 672 | 46 | 10 | 0 | 220 |
| | SqCC | 51 | 523 | 0 | 0 | 166 |
| | SCLC | 0 | 0 | 385 | 0 | 0 |
| | Skeletal muscle | 0 | 0 | 0 | 375 | 0 |

The values represent absolute numbers.

References

1. Cronin, K.A.; Lake, A.J.; Scott, S.; Sherman, R.L.; Noone, A.M.; Howlader, N.; Henley, S.J.; Anderson, R.N.; Firth, A.U.; Ma, J.; et al. Annual Report to the Nation on the Status of Cancer, part I: National cancer statistics. *Cancer* **2018**, *124*, 2785–2800, doi:10.1002/cncr.31551.
2. Bray, F.; Ferlay, J.; Soerjomataram, I.; Siegel, R.L.; Torre, L.A.; Jemal, A. Global cancer statistics 2018: GLOBOCAN estimates of incidence and mortality worldwide for 36 cancers in 185 countries. *CA. Cancer J. Clin.* **2018**, *68*, 394–424, doi:10.3322/caac.21492.
3. Ferlay, J.; Colombet, M.; Soerjomataram, I.; Mathers, C.; Parkin, D.M.; Pineros, M.; Znaor, A.; Bray, F. Estimating the global cancer incidence and mortality in 2018: GLOBOCAN sources and methods. *Int. J. Cancer* **2019**, *144*, 1941–1953, doi:10.1002/ijc.31937.
4. Reck, M.; Rabe, K.F. Precision Diagnosis and Treatment for Advanced Non-Small-Cell Lung Cancer. *N. Engl. J. Med.* **2017**, *377*, 849–861, doi:10.1056/NEJMra1703413.
5. Chen, Z.; Fillmore, C.M.; Hammerman, P.S.; Kim, C.F.; Wong, K.K. Non-small-cell lung cancers: a heterogeneous set of diseases. *Nat. Rev. Cancer* **2014**, *14*, 535–546, doi:10.1038/nrc3775.
6. Santarpia, M.; Aguilar, A.; Chaib, I.; Cardona, A.F.; Fancelli, S.; Laguia, F.; Bracht, J.W.P.; Cao, P.; Molina-Vila, M.A.; Karachaliou, N.; et al. Non-Small-Cell Lung Cancer Signaling Pathways, Metabolism, and PD-1/PD-L1 Antibodies. *Cancers (Basel)* **2020**, *12*, e1475, doi:10.3390/cancers12061475.
7. Warth, A.; Endris, V.; Stenzinger, A.; Penzel, R.; Harms, A.; Duell, T.; Abdollahi, A.; Lindner, M.; Schirmacher, P.; Muley, T.; et al. Genetic changes of non-small cell lung cancer under neoadjuvant therapy. *Oncotarget* **2016**, *7*, 29761–29769, doi:10.18632/oncotarget.8858.
8. Gandhi, L.; Rodriguez-Abreu, D.; Gadgeel, S.; Esteban, E.; Felip, E.; De Angelis, F.; Domine, M.; Clingan, P.; Hochmair, M.J.; Powell, S.F.; et al. Pembrolizumab plus Chemotherapy in Metastatic Non-Small-Cell Lung Cancer. *New Engl. J. Med.* **2018**, *378*, 2078–2092, doi:10.1056/NEJMoa1801005.
9. Reck, M. Pembrolizumab as first-line therapy for metastatic non-small-cell lung cancer. *Immunotherapy* **2018**, *10*, 93–105, doi:10.2217/imt-2017-0121.

10. Reck, M.; Heigener, D.F.; Mok, T.; Soria, J.C.; Rabe, K.F. Management of non-small-cell lung cancer: Recent developments. *The Lancet* **2013**, *382*, 709–719, doi:10.1016/S0140-6736(13)61502-0.
11. Mukhopadhyay, S.; Katzenstein, A.L. Subclassification of non-small cell lung carcinomas lacking morphologic differentiation on biopsy specimens: Utility of an immunohistochemical panel containing TTF-1, napsin A, p63, and CK5/6. *Am. J. Surg. Pathol.* **2011**, *35*, 15–25, doi:10.1097/PAS.0b013e3182036d05.
12. Travis, W.D.; Brambilla, E.; Nicholson, A.G.; Yatabe, Y.; Austin, J.H.M.; Beasley, M.B.; Chirieac, L.R.; Dacic, S.; Duhig, E.; Flieder, D.B.; et al. The 2015 World Health Organization Classification of Lung Tumors: Impact of Genetic, Clinical and Radiologic Advances Since the 2004 Classification. *J. Thorac. Oncol.* **2015**, *10*, 1243–1260, doi:10.1097/JTO.0000000000000630.
13. Adeyi, O.A. Pathology services in developing countries-the West African experience. *Arch. Pathol. Lab. Med.* **2011**, *135*, 183–186, doi:10.1043/2008-0432-CCR.1.
14. Aeffner, F.; Zarella, M.D.; Buchbinder, N.; Bui, M.M.; Goodman, M.R.; Hartman, D.J.; Lujan, G.M.; Molani, M.A.; Parwani, A.V.; Lillard, K.; et al. Introduction to Digital Image Analysis in Whole-slide Imaging: A White Paper from the Digital Pathology Association. *J. Pathol. Inform.* **2019**, *10*, e9, doi:10.4103/jpi.jpi_82_18.
15. Higgins, C. Applications and challenges of digital pathology and whole slide imaging. *Biotech. Histochem.* **2015**, *90*, 341–347, doi:10.3109/10520295.2015.1044566.
16. Grobholz, R. [Digital pathology: The time has come!]. *Pathologe* **2018**, *39*, 228–235, doi:10.1007/s00292-018-0431-0.
17. Unternaehrer, J.; Grobholz, R.; Janowczyk, A.; Zlobec, I.; Swiss Digital Pathology, C. Current opinion, status and future development of digital pathology in Switzerland. *J. Clin. Pathol.* **2019**, *73*, 341–346, doi:10.1136/jclinpath-2019-206155.
18. Lisenko, K.; Leichenring, J.; Zgorzelski, C.; Longuespee, R.; Casadonte, R.; Harms, A.; Kazdal, D.; Stenzinger, A.; Warth, A.; Kriegsmann, M. Qualitative Comparison Between Carrier-based and Classical Tissue Microarrays. *Appl. Immunohistochem. Mol. Morphol.* **2017**, *25*, e74–e79, doi:10.1097/PAI.0000000000000529.
19. Ly, A.; Longuespee, R.; Casadonte, R.; Wandernoth, P.; Schwamborn, K.; Bollwein, C.; Marsching, C.; Kriegsmann, K.; Hopf, C.; Weichert, W.; et al. Site-to-Site Reproducibility and Spatial Resolution in MALDI-MSI of Peptides from Formalin-Fixed Paraffin-Embedded Samples. *Proteom. Clin. Appl* **2019**, *13*, e1800029, doi:10.1002/prca.201800029.
20. Acs, B.; Pelekanou, V.; Bai, Y.; Martinez-Morilla, S.; Toki, M.; Leung, S.C.Y.; Nielsen, T.O.; Rimm, D.L. Ki67 reproducibility using digital image analysis: An inter-platform and inter-operator study. *Lab. Invest.* **2019**, *99*, 107–117, doi:10.1038/s41374-018-0123-7.
21. Bankhead, P.; Fernandez, J.A.; McArt, D.G.; Boyle, D.P.; Li, G.; Loughrey, M.B.; Irwin, G.W.; Harkin, D.P.; James, J.A.; McQuaid, S.; et al. Integrated tumor identification and automated scoring minimizes pathologist involvement and provides new insights to key biomarkers in breast cancer. *Lab. Invest.* **2018**, *98*, 15–26, doi:10.1038/labinvest.2017.131.
22. Song, L.; Liu, J.; Qian, B.; Sun, M.; Yang, K.; Sun, M.; Abbas, S. A Deep Multi-Modal CNN for Multi-Instance Multi-Label Image Classification. *IEEE Trans Image Process.* **2018**, *27*, 6025–6038, doi:10.1109/TIP.2018.2864920.
23. Maruyama, T.; Hayashi, N.; Sato, Y.; Hyuga, S.; Wakayama, Y.; Watanabe, H.; Ogura, A.; Ogura, T. Comparison of medical image classification accuracy among three machine learning methods. *J. Xray Sci. Technol.* **2018**, *26*, 885–893, doi:10.3233/XST-18386.
24. Yatabe, Y.; Dacic, S.; Borczuk, A.C.; Warth, A.; Russell, P.A.; Lantuejoul, S.; Beasley, M.B.; Thunnissen, E.; Pelosi, G.; Rekhtman, N.; et al. Best Practices Recommendations for Diagnostic Immunohistochemistry in Lung Cancer. *J. Thorac. Oncol.* **2019**, *14*, 377–407, doi:10.1016/j.jtho.2018.12.005.
25. Kriegsmann, K.; Zgorzelski, C.; Kazdal, D.; Cremer, M.; Muley, T.; Winter, H.; Longuespee, R.; Kriegsmann, J.; Warth, A.; Kriegsmann, M. Insulinoma-associated Protein 1 (INSM1) in Thoracic Tumors is Less Sensitive but More Specific Compared With Synaptophysin, Chromogranin A, and CD56. *Appl. Immunohistochem. Mol. Morphol* **2020**, *28*, 237–242, doi:10.1097/PAI.0000000000000715.
26. Kriegsmann, K.; Cremer, M.; Zgorzelski, C.; Harms, A.; Muley, T.; Winter, H.; Kazdal, D.; Warth, A.; Kriegsmann, M. Agreement of CK5/6, p40, and p63 immunoreactivity in non-small cell lung cancer. *Pathologe* **2019**, *51*, 240–245, doi:10.1016/j.pathol.2018.11.009.
27. Kriegsmann, M.; Harms, A.; Longuespee, R.; Muley, T.; Winter, H.; Kriegsmann, K.; Kazdal, D.; Goeppert, B.; Pathil, A.; Warth, A. Role of conventional immunomarkers, HNF4-alpha and SATB2, in the differential

- diagnosis of pulmonary and colorectal adenocarcinomas. *Histopathology* **2018**, *72*, 997–1006, doi:10.1111/his.13455.
28. Kriegsmann, M.; Kriegsmann, K.; Harms, A.; Longuespee, R.; Zgorzelski, C.; Leichsenring, J.; Muley, T.; Winter, H.; Kazdal, D.; Goeppert, B.; et al. Expression of HMB45, MelanA and SOX10 is rare in non-small cell lung cancer. *Diagn. Pathol.* **2018**, *13*, e68, doi:10.1186/s13000-018-0751-7.
 29. Mazo, C.; Bernal, J.; Trujillo, M.; Alegre, E. Transfer learning for classification of cardiovascular tissues in histological images. *Comput. Methods Programs Biomed.* **2018**, *165*, 69–76, doi:10.1016/j.cmpb.2018.08.006.
 30. Nishio, M.; Sugiyama, O.; Yakami, M.; Ueno, S.; Kubo, T.; Kuroda, T.; Togashi, K. Computer-aided diagnosis of lung nodule classification between benign nodule, primary lung cancer, and metastatic lung cancer at different image size using deep convolutional neural network with transfer learning. *PLoS ONE* **2018**, *13*, e0200721, doi:10.1371/journal.pone.0200721.
 31. Toratani, M.; Konno, M.; Asai, A.; Koseki, J.; Kawamoto, K.; Tamari, K.; Li, Z.; Sakai, D.; Kudo, T.; Satoh, T.; et al. A Convolutional Neural Network Uses Microscopic Images to Differentiate between Mouse and Human Cell Lines and Their Radioresistant Clones. *Cancer Res.* **2018**, *78*, 6703–6707, doi:10.1158/0008-5472.CAN-18-0653.
 32. Khosravi, P.; Kazemi, E.; Imielinski, M.; Elemento, O.; Hajirasouliha, I. Deep Convolutional Neural Networks Enable Discrimination of Heterogeneous Digital Pathology Images. *EBioMedicine* **2018**, *27*, 317–328, doi:10.1016/j.ebiom.2017.12.026.
 33. Lucas, M.; Jansen, I.; Savci-Heijink, C.D.; Meijer, S.L.; de Boer, O.J.; van Leeuwen, T.G.; de Bruin, D.M.; Marquering, H.A. Deep learning for automatic Gleason pattern classification for grade group determination of prostate biopsies. *Virchows Arch.* **2019**, *475*, 77–83, doi:10.1007/s00428-019-02577-x.
 34. Wang, Y.; Huang, F.; Zhang, Y.; Zhang, R.; Lei, B.; Wang, T. Breast Cancer Image Classification via Multi-level Dual-network Features and Sparse Multi-Relation Regularized Learning. *Conf. Proc. IEEE Eng. Med. Biol. Soc.* **2019**, *2019*, 7023–7026, doi:10.1109/EMBC.2019.8857762.
 35. Cho, S.I.; Sun, S.; Mun, J.H.; Kim, C.; Kim, S.Y.; Cho, S.; Youn, S.W.; Kim, H.C.; Chung, J.H. Dermatologist-level classification of malignant lip diseases using a deep convolutional neural network. *Br. J. Derm.* **2019**, *182*, 1388–1394, doi:10.1111/bjd.18459.
 36. Raimi, K. Illustrated: 10 CNN Architectures. Available online: <https://towardsdatascience.com/illustrated-10-cnn-architectures-95d78ace614d> (accessed on 14 June 2020).
 37. Wang, S.; Yang, D.M.; Rong, R.; Zhan, X.; Fujimoto, J.; Liu, H.; Minna, J.; Wistuba, I.I.; Xie, Y.; Xiao, G. Artificial Intelligence in Lung Cancer Pathology Image Analysis. *Cancers (Basel)* **2019**, *11*, e1673, doi:10.3390/cancers11111673.
 38. Coudray, N.; Ocampo, P.S.; Sakellaropoulos, T.; Narula, N.; Snuderl, M.; Fenyo, D.; Moreira, A.L.; Razavian, N.; Tsirigos, A. Classification and mutation prediction from non-small cell lung cancer histopathology images using deep learning. *Nat. Med.* **2018**, *24*, 1559–1567, doi:10.1038/s41591-018-0177-5.
 39. Iizuka, O.; Kanavati, F.; Kato, K.; Rambeau, M.; Arihiro, K.; Tsuneki, M. Deep Learning Models for Histopathological Classification of Gastric and Colonic Epithelial Tumours. *Sci. Rep.* **2020**, *10*, e1504, doi:10.1038/s41598-020-58467-9.
 40. Gonzalez, D.; Dietz, R.L.; Pantanowitz, L. Feasibility of a deep learning algorithm to distinguish large cell neuroendocrine from small cell lung carcinoma in cytology specimens. *Cytopathology* **2020**, doi:10.1111/cyt.12829.
 41. Gonem, S.; Janssens, W.; Das, N.; Topalovic, M. Applications of artificial intelligence and machine learning in respiratory medicine. *Thorax* **2020**, doi:10.1136/thoraxjnl-2020-214556.
 42. Warth, A.; Stenzinger, A.; von Brunneck, A.C.; Goeppert, B.; Cortis, J.; Petersen, I.; Hoffmann, H.; Schnabel, P.A.; Weichert, W. Interobserver variability in the application of the novel IASLC/ATS/ERS classification for pulmonary adenocarcinomas. *Eur. Respir. J.* **2012**, *40*, 1221–1227, doi:10.1183/09031936.00219211.
 43. Warth, A.; Muley, T.; Herpel, E.; Meister, M.; Herth, F.J.; Schirmacher, P.; Weichert, W.; Hoffmann, H.; Schnabel, P.A. Large-scale comparative analyses of immunomarkers for diagnostic subtyping of non-small-cell lung cancer biopsies. *Histopathology* **2012**, *61*, 1017–1025, doi:10.1111/j.1365-2559.2012.04308.x.
 44. Sauter, G. Representativity of TMA studies. *Methods Mol. Biol.* **2010**, *664*, 27–35, doi:10.1007/978-1-60761-806-5_3.
 45. Steiner, D.F.; MacDonald, R.; Liu, Y.; Truszkowski, P.; Hipp, J.D.; Gammage, C.; Thng, F.; Peng, L.; Stumpe, M.C. Impact of Deep Learning Assistance on the Histopathologic Review of Lymph Nodes for Metastatic Breast Cancer. *Am. J. Surg. Pathol.* **2018**, *42*, 1636–1646, doi:10.1097/PAS.0000000000001151.

46. Kather, J.N.; Pearson, A.T.; Halama, N.; Jager, D.; Krause, J.; Loosen, S.H.; Marx, A.; Boor, P.; Tacke, F.; Neumann, U.P.; et al. Deep learning can predict microsatellite instability directly from histology in gastrointestinal cancer. *Nat. Med.* **2019**, *25*, 1054–1056, doi:10.1038/s41591-019-0462-y.
47. Bulten, W.; Pinckaers, H.; van Boven, H.; Vink, R.; de Bel, T.; van Ginneken, B.; van der Laak, J.; Hulsbergen-van de Kaa, C.; Litjens, G. Automated deep-learning system for Gleason grading of prostate cancer using biopsies: A diagnostic study. *Lancet. Oncol.* **2020**, *21*, 233–241, doi:10.1016/S1470-2045(19)30739-9.
48. Gertych, A.; Swiderska-Chadaj, Z.; Ma, Z.; Ing, N.; Markiewicz, T.; Cierniak, S.; Salemi, H.; Guzman, S.; Walts, A.E.; Knudsen, B.S. Convolutional neural networks can accurately distinguish four histologic growth patterns of lung adenocarcinoma in digital slides. *Sci. Rep.* **2019**, *9*, e1483, doi:10.1038/s41598-018-37638-9.
49. Singh, R.; Ahmed, T.; Kumar, A.; Singh, A.K.; Pandey, A.K.; Singh, S.K. Imbalanced Breast Cancer Classification Using Transfer Learning. *IEEE/ACM Trans. Comput. Biol. Bioinform.* **2020**, doi:10.1109/TCBB.2020.2980831.
50. Chen, Z.; Xu, T.B.; Du, C.; Liu, C.L.; He, H. Dynamical Channel Pruning by Conditional Accuracy Change for Deep Neural Networks. *IEEE Trans. Neural Netw. Learn. Syst* **2020**, doi:10.1109/TNNLS.2020.2979517.
51. Frazier-Logue, N.; Hanson, S.J. The Stochastic Delta Rule: Faster and More Accurate Deep Learning Through Adaptive Weight Noise. *Neural Comput.* **2020**, *32*, 1018–1032, doi:10.1162/neco_a_01276.
52. Liu, Y.; Kohlberger, T.; Norouzi, M.; Dahl, G.E.; Smith, J.L.; Mohtashamian, A.; Olson, N.; Peng, L.H.; Hipp, J.D.; Stumpe, M.C. Artificial Intelligence-Based Breast Cancer Nodal Metastasis Detection: Insights Into the Black Box for Pathologists. *Arch. Pathol. Lab. Med.* **2019**, *143*, 859–868, doi:10.5858/arpa.2018-0147-OA.
53. Guo, Z.; Liu, H.; Ni, H.; Wang, X.; Su, M.; Guo, W.; Wang, K.; Jiang, T.; Qian, Y. A Fast and Refined Cancer Regions Segmentation Framework in Whole-slide Breast Pathological Images. *Sci. Rep.* **2019**, *9*, e882, doi:10.1038/s41598-018-37492-9.
54. Ehteshami Bejnordi, B.; Veta, M.; Johannes van Diest, P.; van Ginneken, B.; Karssemeijer, N.; Litjens, G.; van der Laak, J.; the, C.C.; Hermesen, M.; Manson, Q.F.; et al. Diagnostic Assessment of Deep Learning Algorithms for Detection of Lymph Node Metastases in Women With Breast Cancer. *JAMA.* **2017**, *318*, 2199–2210, doi:10.1001/jama.2017.14585.
55. Bandi, P.; Geessink, O.; Manson, Q.; Van Dijk, M.; Balkenhol, M.; Hermesen, M.; Ehteshami Bejnordi, B.; Lee, B.; Paeng, K.; Zhong, A.; et al. From Detection of Individual Metastases to Classification of Lymph Node Status at the Patient Level: The CAMELYON17 Challenge. *IEEE Trans. Med. Imaging* **2019**, *38*, 550–560, doi:10.1109/TMI.2018.2867350.
56. Komura, D.; Ishikawa, S. Machine Learning Methods for Histopathological Image Analysis. *Comput. Struct. Biotechnol. J.* **2018**, *16*, 34–42, doi:10.1016/j.csbj.2018.01.001.
57. Wei, J. Classification of Histopathology Images with Deep Learning. Available online: <https://medium.com/health-data-science/classification-of-histopathology-images-with-deep-learning-a-practical-guide-2e3ffd6d59c5> (accessed on 14 June 2020)
58. Zhang, J.T.; Li, Y.; Yan, L.X.; Zhu, Z.F.; Dong, X.R.; Chu, Q.; Wu, L.; Zhang, H.M.; Xu, C.W.; Lin, G.; et al. Disparity in clinical outcomes between pure and combined pulmonary large-cell neuroendocrine carcinoma: A multi-center retrospective study. *Lung Cancer* **2020**, *139*, 118–123, doi:10.1016/j.lungcan.2019.11.004.
59. Lin, M.W.; Su, K.Y.; Su, T.J.; Chang, C.C.; Lin, J.W.; Lee, Y.H.; Yu, S.L.; Chen, J.S.; Hsieh, M.S. Clinicopathological and genomic comparisons between different histologic components in combined small cell lung cancer and non-small cell lung cancer. *Lung Cancer* **2018**, *125*, 282–290, doi:10.1016/j.lungcan.2018.10.006.

